Biosensors and Bioelectronics 302 (2026) 118517

Contents lists available at ScienceDirect

Biosensors and Bioelectronics

journal homepage: www.elsevier.com/locate/bios

Multimodal activity-affinity assay of ADAM-10 extracellular vesicles in untreated plasma reveals metastatic stage of colorectal cancer

Tiger Haoran Shi [a,1], John Alex Sinclair [a,1], Youwen Zhang [a], Xuemin Lu [b], Sonu Kumar [a], Xin Lu [b], Satyajyoti Senapati [a], Hsueh-Chia Chang [a,*]

[a] Department of Chemical and Biomolecular Engineering, University of Notre Dame, Indiana, 46556, USA
[b] Department of Biological Sciences, University of Notre Dame, Indiana, 46556, USA

ARTICLE INFO

Keywords:
Extracellular vesicles
Metastasis
Colorectal cancer
Metalloproteinase
Janus particle
Machine learning

ABSTRACT

Metalloproteinases (MPs) such as a-disintegrin and metalloproteinase-10 (ADAM-10) are key drivers of extracellular matrix remodeling during tumor progression, yet MP-based liquid biopsy tests have not reached clinical utility. Here, we show that active ADAM-10 is selectively enriched on the surface of circulating extracellular vesicles (EVs) in the plasma of colorectal cancer patients. Our findings further suggest ADAM-10+ EVs are locally enriched in dense pre-metastatic tumor extracellular matrices and subsequently accumulate in blood post-metastasis. To capture these unique signatures of disease progression, an ADAM-10 activity assay is integrated with a novel size-sensitive Immuno-Janus Particle affinity assay for characterizing ADAM-10+ EVs in untreated plasma. In a 43-patient colorectal cancer cohort, this multimodal platform distinguishes healthy, pre-metastatic, and metastatic states with 95% overall accuracy. When combined with lipidomics as a third modality, the platform correctly determines 97.4% cancer stage accuracy, with only one misclassification. This study establishes a multimodal EV-based activity/affinity assay as a robust framework for liquid biopsy, providing accurate cancer staging, improved prognostics, and offering a potential platform for pan-disease diagnostics.

1. Introduction

Colorectal cancer (CRC) remains a leading cause of cancer mortality, with current diagnostics favoring solid tumor detection at advanced stages. Prognostic outlooks decline precipitously following metastasis to distal organs, with 5-year survival rates falling to 10-20% (Crosby et al., 2022; Guan, 2015; Survival Rates for Colorectal Cancer, 2025; U.S. Cancer Statistics Colorectal Cancer Stat Bite, 2025). This presents an unmet need for a minimally invasive, repeatable screening technique capable of identifying pre-metastatic tumors, defined here as tumors that have spread no further than the regional lymph nodes or surrounding tissues. Liquid biopsy techniques that analyze circulating biomolecules and bionanoparticles offer a promising, non-invasive, high-throughput alternative to stool tests and colonoscopy, which face challenges in early-stage sensitivity, and invasiveness (Cavallaro et al., 2019; Chen et al., 2020; Kalluri and LeBleu, 2020; Kottorou et al., 2023; Sabatke et al., 2023). However, a tool for characterizing these information-dense molecular carriers that can differentiate between metastatic states has not yet been reported.

Extracellular vesicles (EVs) are a class of lipid-bilayer enclosed nanovesicles secreted by nearly all cell types. They transport proteins, nucleic acids, and metabolites that reflect the origin and condition of their parent cell, including cancer-associated changes (Cavallaro et al., 2019; Kalluri and LeBleu, 2020; Kottorou et al., 2023; Li et al., 2023; Sabatke et al., 2023). Tumor-derived EVs circulate abundantly in blood plasma, serving as mediators in tumor progression, metastasis, and microenvironment remodeling (Gao and Li, 2023; Xiong et al., 2020; Zheng et al., 2019). The shift of EV cargo towards pro-tumorigenic inflammatory signaling molecules (Abusamra et al., 2005; Costa-Silva et al., 2015; Fabbri et al., 2012; Shao et al., 2018; Wu et al., 2016) and extracellular matrix (ECM)-modifying enzymes (Moshrefiravasjani et al., 2024; Spugnini et al., 2018; Zhao et al., 2016) makes EVs attractive carriers for established cancer biomarkers. We previously demonstrated that EV-bound proteins such as aEGFR, GPC1, and CEA enable highly accurate cancer site classification, yielding AUC values of 0.92-0.99 (Kumar et al., 2025).

* Corresponding author. Department of Chemical and Biomolecular Engineering, University of Notre Dame, Notre Dame, IN, 46556, USA.
E-mail address: hchang@nd.edu (H.-C. Chang).
[1] Denotes Equal Author Contribution.

https://doi.org/10.1016/j.bios.2026.118517
Received 9 September 2025; Received in revised form 19 January 2026; Accepted 10 February 2026
Available online 11 February 2026

Another EV-associated class of biomarkers, metalloproteinases (MPs) are of particular interest. These redox-reactive enzymes regulate ECM remodeling and are linked to tumor growth and inflammation (Cai et al., 2022; Clark et al., 2008; Cox, 2021). A-disintegrin and metalloproteinase-10 (ADAM-10) is a membrane-affixed MP, which is transferred to EVs where they promote vesicle biogenesis, ECM degradation, and migratory signaling, facilitating cancer progression (Aljohmani et al., 2022; Hakulinen et al., 2008; Keller et al., 2020). In a healthy human body, ADAM-10 – particularly those anchored on the surface of extracellular vesicles (EVs) – serves to modulate and maintain homeostasis of tissue surface proteins, solubilization of immune regulators, and cell adhesion behaviors through ectodomain shedding of several species of membrane proteins (Orme et al., 2020; Rosenbaum and Saftig, 2024). These molecules are largely produced by healthy skin, hair, and immune cells to regulate cell communication, migration, and first-line immune response (Maretzky et al., 2008; Sakamoto et al., 2021) and by healthy astrocytes in the brain to regulate amyloid precursor protein (APP) (Elsworthy et al., 2022; Yuan et al., 2017). In cancer cells, increased ADAM-10 expression and activity have been indicated to have direct action in the progression towards metastasis and chemoresistance in colorectal cancer (CRC). This is caused by its direct cleavage of signaling molecules such as NOTCH (Saha et al., 2023), L1-CAM (Gavert et al., 2007), and EGFR/ErbB ligand (Dempsey, 2017) on tumor cells and surrounding cells. These modifications lead to increased cancer cell proliferation through Wnt pathway signaling (Xiang et al., 2025) and increased metastatic capacity through removal of the ectodomains of cell adhesion receptor L1-CAM (Gavert et al., 2007). Although soluble forms of ADAM-10 are abundant in plasma, their enzymatic activity and contribution to metastatic progression are significantly lower than those of EV-bound MPs (Pelegrini et al., 2025). Inactive ADAM-10 is depleted from the cell surface (Seifert et al., 2021), while EV-bound ADAM-10 remains largely active, situating it as a functional biomarker for mapping cancer evolution. However, existing assays typically measure either total enzymatic activity or total protein content. Although activity-specific methods relay key physiological behavior, they are highly sensitive to sample handling and require extensive isolation steps in addition to well-designed reporter substrates (Fang et al., 2021; Zhang et al., 2020). Conversely, affinity-based assays quantify total ADAM-10 but are blind to enzymatic state and EV association, often lacking the sensitivity to resolve specific EV subsets (Maniya et al., 2024). Moreover, ADAM-10 dysregulation is present in numerous afflictions, including wound healing and neurodegenerative diseases (Khezri et al., 2023), so ADAM-10 assays are not sufficient as an independent cancer screening test. They can, however, complement EV-based biomarker assays, including our own (Cheng et al., 2025; Kumar et al., 2024, 2025; Maniya et al., 2024; Safavi-Sohi et al., 2025; Sharma et al., 2023, 2025), which can collectively provide cancer site specificity. In patients with a known diagnosis, such as CRC, ADAM-10 activity may serve to support prognostic assessment or therapeutic response, which will be explored in this paper.

In this study, we present a parallel activity-affinity assay of ADAM-10 which integrates an established ADAM-10 activity assay with a separate, orthogonal Immuno-Janus Particle (IJP) assay (Kumar et al., 2025). This novel assay combination capably quantifies relative ADAM-10+ EV abundance and its associated activity directly in plasma. Selecting IJPs for ADAM-10+ EV normalization over alternative EV-centric diagnostic technologies hinges on several key advantages detailed in our prior work (Kumar et al., 2025). Primarily, the IJPs resist common fouling proteins like albumin, which are many orders of magnitude ($> 10^9$) more concentrated than the target ADAM-10+ EVs. Most existing EV-diagnostic technologies rely on a lengthy isolation step (ultracentrifugation (UC), ultrafiltration (UF), or chromatography) prior to characterization that is prone to pre-treatment biases and sample loss. As the IJP platform circumvents the need for isolation by design, the technology enabled rapid, direct detection within a large population of untreated patient plasma samples. Using progressive CRC patient plasma (Table 1) and four prostate cancer cell lines, we show that ADAM-10 activity localizes predominantly on EVs and that the abundance, size, and activity of ADAM-10+ EVs differ considerably between healthy, pre-metastatic, and metastatic patients. To enhance diagnostic performance, we implemented lipidomic analysis using Nile Red lipid dye as a third metric. We find that the bimodal approach achieves 95%

Table 1
Clinical cohort demographics information.

	Cohort	Healthy	Pre-Metastatic	Metastatic		Total
Age (years)						
	<60	0	3	7	=	10
	≥60 and < 70	16	4	2	=	22
	≥70	0	5	5	=	10
Sex						
	Male	6	5	11	=	22
	Female	10	7	4	=	21
BMI						
	<18.5	-	0	1	=	1
	≥18.5 and < 25	-	2	3	=	5
	≥25 and < 30	-	5	4	=	9
	≥30	-	4	3	=	7
	No Data	16	1	4	=	21
Smoking Status						
	Never Smoked	-	4	6	=	10
	Former Smoker	-	4	4	=	8
	Current Smoker	-	1	4	=	5
	No Data	16	3	1	=	20
Stage at Diagnosis						
	I	-	1	0	=	1
	II	-	5	4	=	9
	III	-	5	3	=	8
	IV	-	0	8	=	8
Treatment History						
	Treatment Naive	-	5	2	=	7
	Surgery	-	3	6	=	9
	Systemic	-	5	13	=	18
	Radiation	-	3	6	=	9

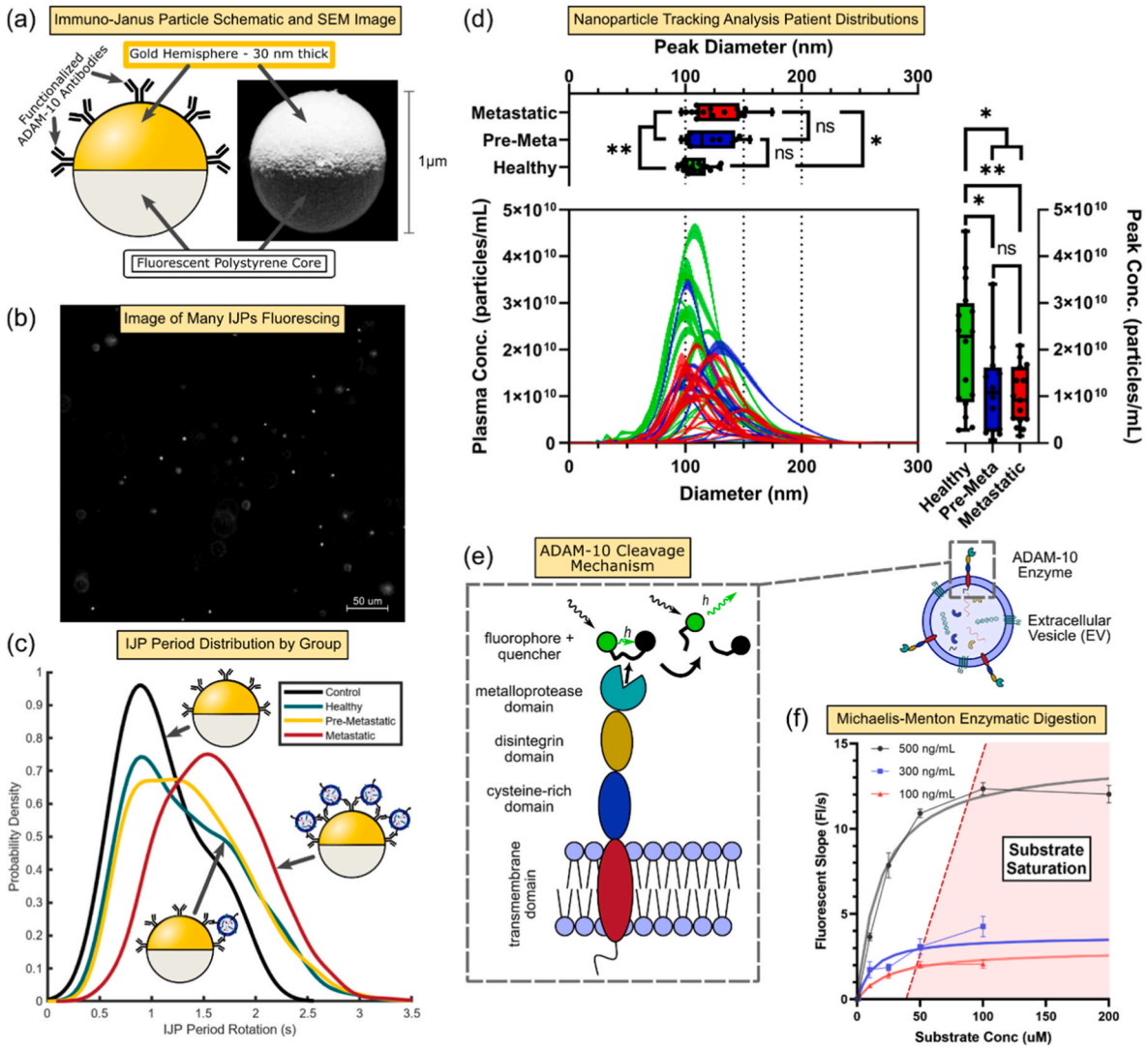

Fig. 1. Overview of assays conducted in parallel for characterizing ADAM-10+ EVs. (a) Schematic of an Immuno-Janus Particle (IJP) alongside an SEM image. The fluorescent polystyrene core and a 30 nm gold hemisphere for antibody conjugation enable anisotropic fluorescence. (b) Fluorescence image of IJPs in PBS (546 nm excitation, 10x), showing intensity variation from orientation-dependent emission. (c) Probability distribution function of anti-ADAM-10 IJP rotational periods after incubation with PBS control (1.10s) or plasma from healthy (1.34s), pre-metastatic (1.38s), and metastatic (1.61s) patients. Schematics illustrate the increasing EV binding impacting the rightward shift in period. (d) Nanoparticle tracking analysis (NTA) distributions for 43 patient plasma samples (0.22 µm filtered). The central plot represents the particle size-concentration distributions, the top panel represents sample peak particle diameter, and the right panel represents the concentration at each sample's distribution maxima. Significance values determined using Welch's *t*-Test. (e) Schematic of EV-bound, enzymatically active ADAM-10 cleaving a synthetic peptide-based molecular beacon. (f) Michaelis-Menten kinetics plot of beacon digestion by variable concentration recombinant human ADAM-10 (rhADAM-10), yielding fluorescence over time. (For interpretation of the references to color in this figure legend, the reader is referred to the Web version of this article.)

overall metastatic potential accuracy and 89.4% staging accuracy, while the trimodal approach achieves 100% overall metastatic potential accuracy and 97.4% staging accuracy.

These findings establish EV-bound ADAM-10 activity as a meaningful indicator of disease progression and demonstrate that combining activity and affinity measurements on EVs can achieve clinically relevant staging accuracy. Furthermore, integrating ADAM-10 with an expanded EV biomarker library could form the groundwork for a massively multiplexed assay capable of characterizing distinct tumor phenotypes to progress towards a comprehensive pan-cancer liquid biopsy platform.

2. Results and discussion

2.1. Immuno-Janus Particles capture and report ADAM-10+ vesicles

To quantify ADAM-10+ EVs, we implement our novel Immuno-Janus Particle (IJP) (Kumar et al., 2025) sensor. The IJPs are 1000-nm fluorescent polystyrene beads coated with a 30 nm golden hemisphere, which anisotropically suppresses the fluorescence when oriented towards the viewer (Fig. 1a). The gold surface can facilely conjugate a variety of antibodies, including α-ADAM-10. When these particles undergo chaotic thermal fluctuations in solution, they rotate freely and exhibit an observable blinking phenomenon (Fig. 1b). The blinking frequency is inversely related to particle size, represented by the rotational diffusivity $D_r = \frac{k_b T}{\pi \mu d_p^3} = \frac{1}{2}\cdot\frac{\Delta\theta^2}{\Delta t}$. The cubic dependence on particle diameter means that the rotational diffusivity decreases precipitously with increasing size. In contrast, translational diffusivity scales inversely ($D_R \propto d_p^{-1}$), enabling the rotational frequency to be highly sensitive relative to the translation motion. This size sensitivity not only provides precise quantification of the effective size increase due to EV binding but also reduces noise from dispersed ADAM-10 with a much smaller size than EVs. By observing the relative blink rates, we can approximate the

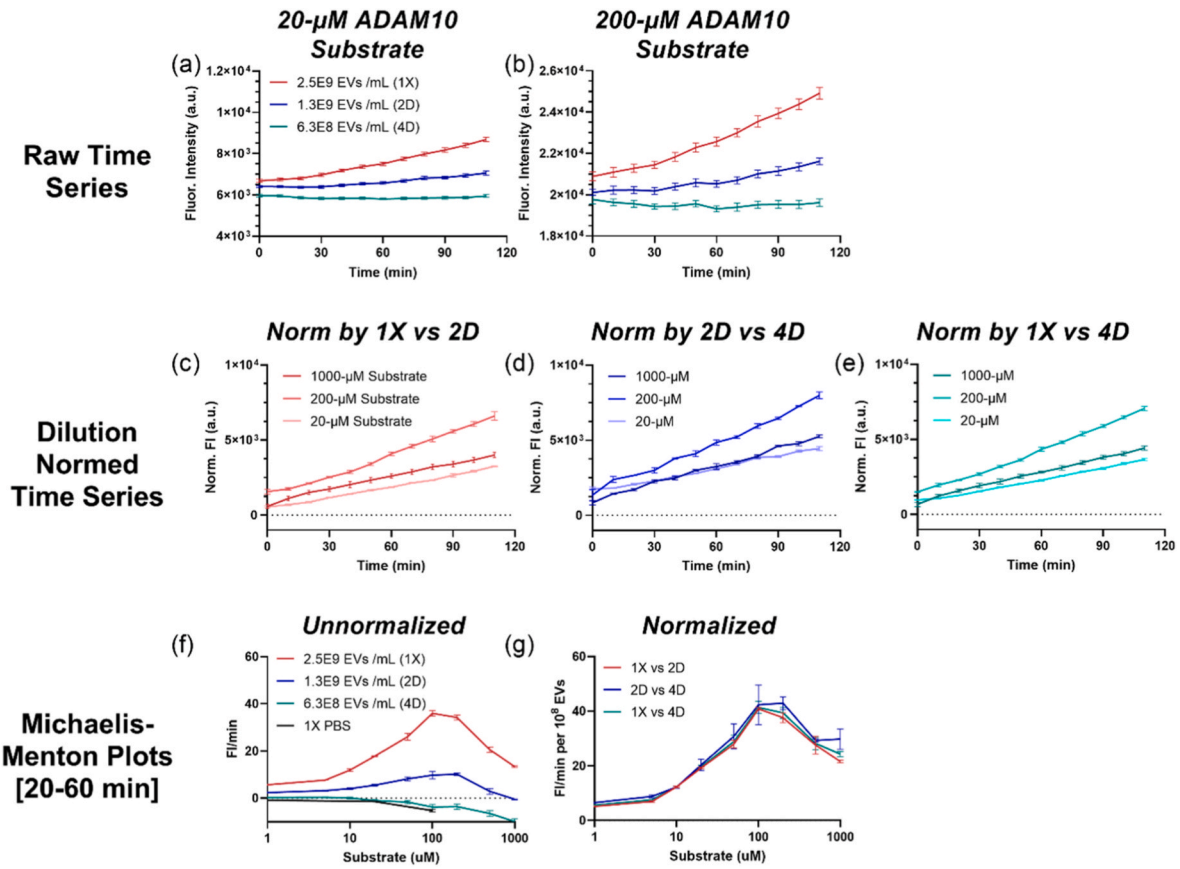

Fig. 2. Dilution normalization of bulk activity assay fluorescent evolution time series of EV-associated ADAM-10. (a-b) Fluorescent signal evolution curves for activity-based assays at varying concentrations of ADAM-10+ EVs derived from healthy human plasma samples for (a) 20-μM and (b) 200-μM of ADAM-10 specific activity substrate. (c-e) Internally normalized fluorescent evolution curves using serial dilutions of samples for various applied concentrations of ADAM-10 specific activity substrates, where the samples are normalized (c) 1X to 2D dilution, (d) 2D to 4D dilution, and (e) 1X to 4D dilution. (f-g) Michaelis-Menten plots for fitted slopes of time series data of (f) unnormalized and (g) normalized curves. Slopes are fitted for times series data at 20-60 min after start of experiment at 10-min time steps. All error bars represent measured or propagated standard errors of means.

effective size of each tracked particle. Irreversible EV-IJP binding expands the hydrodynamic particle diameter with the number of EVs and the size of the bound EVs. The blinking frequency of IJP is hence a sensitive and selective metric for ADAM-10+ EV number and size (Fig. 1c).

A custom single-particle tracking software captures the blinking dynamics of each detected IJP over the course of a 120 s recording (Supporting Fig. 1). This figure displays the trajectory of all tracked IJPs, with green representing early tracks, and red representing late tracks. From these data, ensemble particle time periods are extracted and combined following continuous wavelet transformations are applied on all valid IJPs. Fig. 1c shows probability distribution functions of the control group and three progressive metastatic stages. Each curve aggregates all IJP period measurements for every patient within their respective cohort, constituting thousands of IJPs and illustrating the increasing upregulation of ADAM-10+ EVs throughout CRC progression, with metastatic cancers having a significant increase in IJP blinking period.

The NTA distributions (Fig. 1d) reveal cohort-level trends in particle concentration and size. We found particle diameters are significantly increased in CRC patient populations as compared to the healthy population ($p = 0.0063$), with shifts upward in peak particle diameters noted primarily from the metastatic population ($p = 0.0164$). Additionally, we noted the reduction of peak concentrations in CRC patient populations as compared to the healthy population ($p = 0.0124$), with significant decreases noted from both pre-metastatic ($p = 0.0456$) and metastatic patients ($p = 0.0088$). These shifts suggest a potential redistribution of vesicle subpopulations from small EV profiles (sEVs) towards larger EVs (lEVs), which aligns with our prior observations (Cheng et al., 2025).

2.2. *Off-target interference of ADAM-10 activity can be normalized through serial dilution*

To assess total enzymatic activity, we adapted a digestible fluorophore peptide beacon based on the (PRAEALKGGK) sequence from prior work (Chen et al., 2021). The beacon consists of a 5-FAM fluorophore and a peptide-adjacent DABCYL quencher, so that the proteolytic cleavage emits a measurable fluorescent signal, as shown in Fig. 1e. Soluble and membrane-bound ADAM-10 are both capable of cleaving this substrate. This fluorescent growth over time is determined by classical Michaelis-Menten kinetics defined by the rate law $V_0 = V_{MAX}\frac{[S]}{[S]+K_M}$, where V_0 is the initial reaction rate, $V_{MAX} = k_{cat}\cdot([E]+[ES]) = k_{cat}\cdot[E]_0$ is the maximum reaction rate, and $[S]$ is the peptide substrate concentration. K_M is the Michaelis constant, defined by $K_M = \frac{[E][S]}{[ES]}$ with $[E]$ and $[ES]$ being enzyme and enzyme-substrate complex concentrations, respectively (Van Daela and Nopens, 2015). At high applied concentration of substrate [S], the rate equation simplifies to $V_0 = V_{Max} = k_{cat}\cdot[E]_0$ and is linear with respect to the total concentration of enzymes in the system. Using three concentrations of recombinant human ADAM-10 (rhADAM-10) in Fig. 1f, a substrate concentration of 100 μM was selected as optimal since it lies wholly within this saturation region, allowing us to attribute any

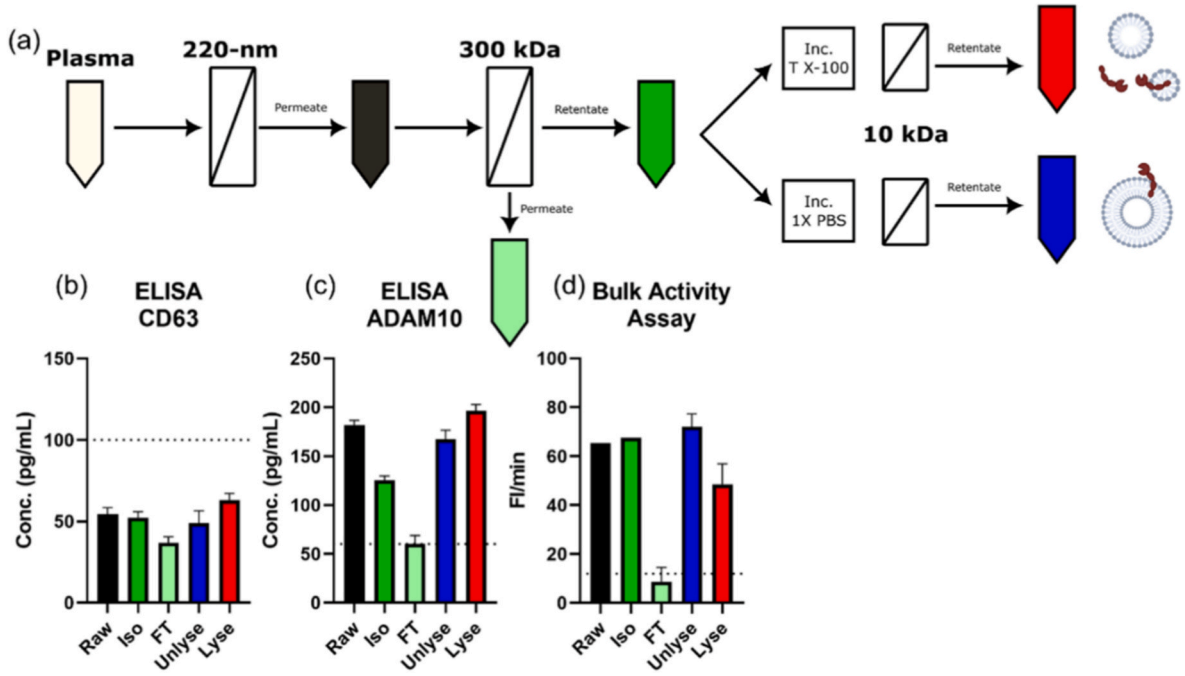

Fig. 3. ELISA and bulk activity assay of healthy human plasma fractions. (a) Sequential filtration workflow of healthy human plasma. Samples filtered through a 220 nm syringe filter, and a 300 kDa filter. The 300 kDa retentate (vesicle-rich fraction) was either lysed with 0.10 wt% final concentration Triton X-100 or washed with PBS before removing small components with a 10 kDA filter. Colors shown here are maintained for subsequent panels. (b) CD63 ELISA quantification shows low signal across all five plasma fractions. (c) ADAM-10 ELISA quantification shows detectable signals for all plasma fractions except the 300 kDa permeate (vesicle-free fraction), suggesting vesicle-associated quantification. (d) Bulk ADAM-10 activity assay mirrors trends found in ADAM-10 ELISA for the five plasma fractions, with low activity for the 300 kDa filter permeate, and high signal in vesicle-containing fractions. (For interpretation of the references to color in this figure legend, the reader is referred to the Web version of this article.)

changes in reaction rate solely to differences in enzyme concentration.

When subjected to human plasma, the fluorescent time series (Fig. 2a and b) appear non-linear until after an hour of reaction initiation. With this skewed data, the resultant Michaelis-Menton plots (Fig. 2e) appear non-standard. This is due to the interference with the fluorescein (5-FAM) molecule. It is known that free-radicals and peroxides in blood can destructively, dynamically quench fluorescein as is the mechanism behind the oxygen radical absorbance capacity (ORAC) assay (Gunawardena et al., BMC Res. Notes, 2019). As we perform our experiments at a consistent concentration that is in high excess of the fluorescent activity substrate, the extant free-radical species become depleted by a consistent background curvature and the time evolution ceases to decrease. As this mechanism is independent of the molecular beacon digestion reaction, this background curve can be reliably removed through the dilution normalization (Fig. 2c–e). The Michaelis-Menton plot featuring normalized reaction rate for a variety of different levels of dilution (Fig. 2f) demonstrates the convergence of each normalization to the underlying reaction rate while removing interfering noise from the sample. Using this methodology, subsequent activity assays can be internally normalized without extensive sample processing and cleaning. This technique does not aim to resolve interference from direct or indirection inhibitors of ADAM-10 activity. However, it is not necessary to correct these types of interference. We are not aiming to quantify the exact number of ADAM-10 molecules in each plasma matrix, rather we are aiming to measure the effective ADAM-10 activity which would include effects of competitive, non-competitive, and uncompetitive inhibition.

2.3. *ADAM-10+ vesicles enhance enzymatic activity*

To test the dependence of ADAM-10 activity on its location on the EV membrane, the workflow illustrated in Fig. 3a was implemented. Healthy human plasma was filtered through 220-nm filter to remove cell debris and large vesicles. The permeate (Raw) is passed through a 300 kDa centrifugal filter where the twice-filtered permeate (FT) contains the free-floating protein fraction while the retentate (Iso) retains the plasma vesicles (<220 nm) such as EVs. The EV isolate (Iso) was reconstituted to the original sample volume using 1X PBS and split into two equal 150-μL fractions: (1) one sample was given 350-μL of 0.15% Triton X-100 surfactant (Lyse) for a final concentration of 0.10 wt%, and (2) the other control sample received 350-μL of 1X PBS (Unlyse). Both samples were incubated for 30 min at room temperature on an orbital shaker and subsequently washed in a 10-kDa centrifugal spin filter with three resuspensions of 400-μL 1X PBS to remove remaining surfactant. The samples were each resuspended in 400-μL of 1X PBS. All samples (Raw, Iso, FT, Unlyse, & Lyse) were assayed using total CD63 ELISA, total ADAM-10 ELISA, and bulk ADAM-10 activity assay.

Looking at the ELISA results (Fig. 3b), we find that CD63 was too low in concentration in all samples to be quantified. At the Raw and Unlyse samples, the ADAM-10 concentration and activity were retained in the EV through the 300 kDa and 10 kDa spin filtering steps (Fig. 3c and d). Along with this, despite the apparent drop in ADAM-10 concentration for the Iso sample, the activity rate is retained. This behavior suggests that the drop is likely due to aggregation of nano-carriers in the spin-filtering rather than a true loss in enzyme concentration. Additionally, we notice that for both ADAM-10 concentration and activity rate the FT fraction containing the free-floating proteins holds no detectable level of ADAM-10 presence or activity (Fig. 3c and d). Ultimately, upon lysis of the nano-carriers in the sample, we notice a 10% increase in ADAM-10 concentration and a simultaneous 35% reduction in ADAM-10 activity rate. The above results suggest that ADAM-10 in healthy plasma is primarily located on the surface of nano-carriers such as EVs. Furthermore, delipidation of ADAM-10+ EVs releases a small additional amount of ADAM-10 into solution (Fig. 3c), yet this causes a significant reduction in enzymatic activity (Fig. 3d). These findings suggest that ADAM-10 activity is enhanced when embedded in a lipid membrane, likely due

to the anchored domain securing the enzyme's structure (Pelegrini et al., 2025). Disrupting this membrane system increases the amount of solubilized protein, as the internal cargo is jettisoned into the bulk. However, this disruption destabilizes the membrane proteins leading to reduced activity. As such, the ADAM-10 species of highest enzymatic function, and the ideal species to analyze from hereon are intact EVs. These trends were verified for 220-nm filtered cell cultured media (CCM) produced by patient-derived healthy human dermal cells as well (Supporting Fig. 2). These cells were shown to inherently produce high ADAM-10 activity on their EVs. Although ADAM-10 enzymatic activity is not explicitly EV-specific, the negligible activity contributed by soluble forms of ADAM-10 empirically conclude that ADAM-10 activity signals from untreated plasma and cell-culture sources are EV-specific.

2.4. *ADAM-10 signal is expressed primarily on EVs and correlates with metastatic state in prostate cancer cell cultures*

ADAM-10 *in vitro* studies link its overexpression to increased metastasis in colon, gastric, prostate, ovarian, uterine, and leukemia cancer cell cultures (Saha et al., 2023), underscoring its entanglement with cancer progression. Subsequently, we applied this enzymatic activity assay to prostate cancer (PCa) cell lines of varying metastatic potential, including LNCaP, 22Rv1, DU145, and PC3, evaluating both cell culture media and ultracentrifugation (UC) isolated EVs (Supporting Fig. 4d). Here, we used androgen sensitivity as a proxy metric for disease progression, where prostate cancer cells become more insensitive to androgen deprivation therapy as the disease progresses towards later stages. A general trend emerged where androgen-insensitive cell lines exhibit a higher EV-normalized enzymatic activity, with the exception of 22Rv1, showing markedly lower enzymatic digestion. Akin to the plasma results, enzymatic activity rates were consistent across both unprocessed media and isolated EVs. These findings support a model where the enzymatically relevant ADAM-10 is confined to EV membranes. Pairing the IJP platform, which is independently capable of quantifying ADAM-10+ EVs, allows us to gain a dual-modality screening technique. One test quantifies vesicle abundance and the other quantifies enzymatic capacity, offering dynamic insight into cancer-related vesicle heterogeneity through the oncogenic process. As shown in

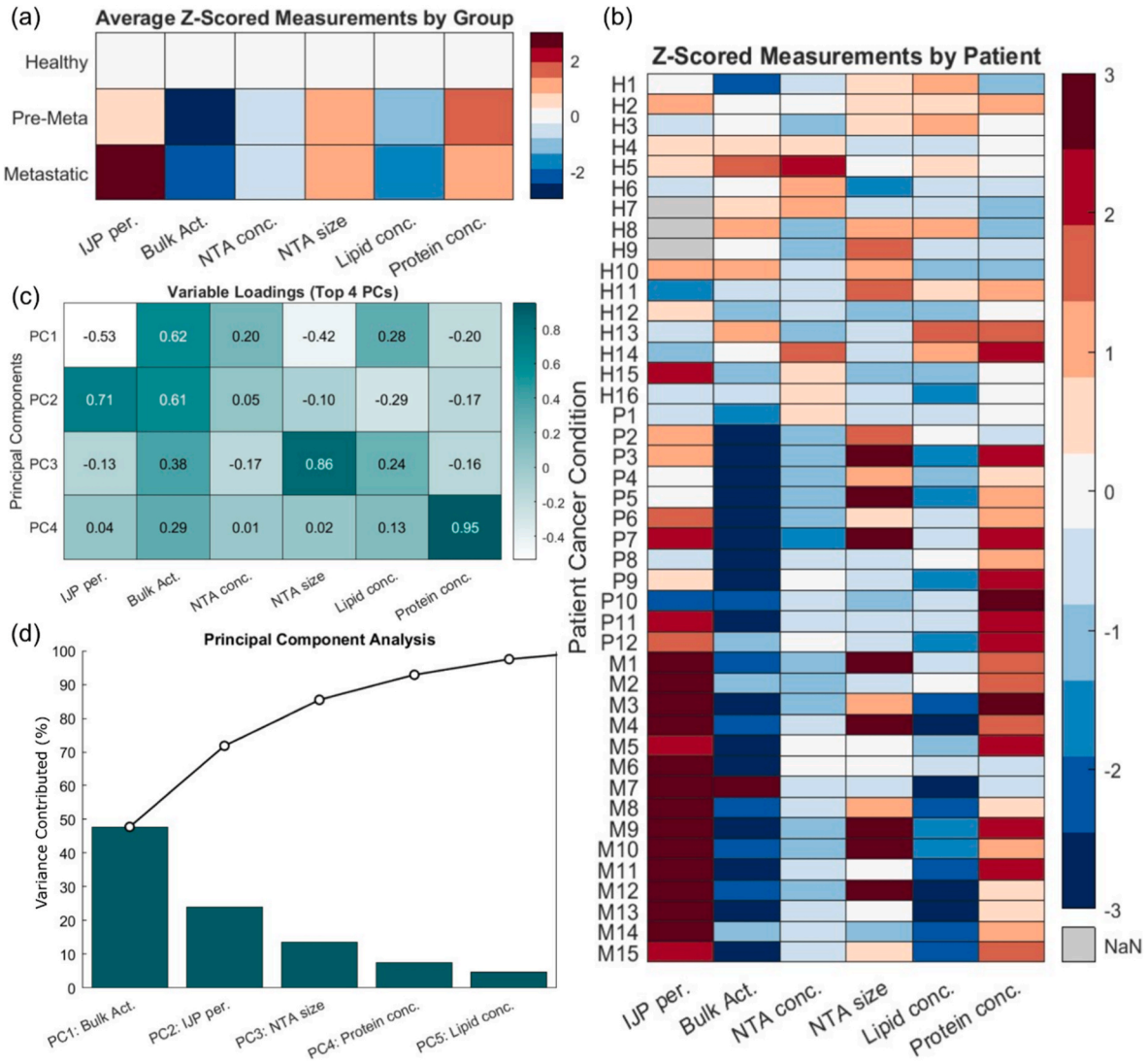

Fig. 4. Multimodal plasma profiling and diagnostic classification using Z-score normalizations and principal component analysis. (a) Heatmap of group-averaged Z-scores for six parameters: Immuno-Janus Particle (IJP) rotational period, bulk ADAM-10 activity, nanoparticle tracking analysis (NTA) particle concentration, NTA mean particle diameter, plasma lipid content (Nile Red fluorescence), and total protein content. Values normalized to the healthy cohort mean. (b) Heatmap of individual patient Z-scores; gray cells indicate unmeasured parameters. (c) Variable loading heatmap showing the contributions of each parameter to the top four principal components (PCs) derived from PCA. Color grading reflects magnitude and direction of loadings. (d) Pareto plot showing variance explained by each PCs and their respective top-loading variable. (For interpretation of the references to color in this figure legend, the reader is referred to the Web version of this article.)

Fig. 3d, the raw plasma filtered through a 220 nm membrane produces comparable enzymatic signals to higher purity vesicle fractions (300 kDa retentate and 10 kDa PBS washed retentate). Combining this fact with the IJP platform's immunity to soluble protein interference, this motivates our use of minimally processed plasma in our subsequent EV-centric activity/affinity analyses. We implement both enzymatic and IJP assays to a pilot study of 43 patient sample cohorts, alongside additional orthogonal characterization.

2.5. *Unsupervised learning to determine parameters with diagnostic efficacy*

The comprehensive plasma analysis consists of six orthogonal measurements: bulk ADAM-10 enzymatic activity, Immuno-Janus Particle rotational period to measure ADAM-10+ extracellular vesicle concentration, NTA-derived particle concentration, NTA-derived mean particle diameter, plasma lipid content quantified by Nile Red staining, and total protein concentration measured by Bradford assay.

Because these metrics span disparate numerical scales (e.g., IJP period: 1.16-1.73 s, and nanovesicle concentration: $3.51\times 10^{10} - 2.44\times 10^{12}$ particles/mL), raw values were converted Z-scores relative to the healthy cohort mean values:

$$z_i = \frac{x_i - \mu_{healthy}}{\sigma_{healthy}}$$

Group-averaged Z-scores are shown in Fig. 4a, and individual patient expression in Fig. 4b. We observe a single metastatic outlier (M7) whose expression levels are inconsistent among group behavior for most analyzed parameters, save IJP period. The sample's aberrant viscosity, color, and turbidity suggest likely hemolysis during plasma preparation (Sowemimo-Coker, 2002). Across disease progression from healthy to metastatic states, we observe increased IJP period, particle size, and protein concentration, contrasted against a decreased ADAM-10 activity, particle concentration, and lipid content. These trends are not strictly linear; for example, total protein concentration plateaus in pre-metastatic cancer, before declining in metastatic patients. Non-linearity suggests attributes are highly specific to their respective stage.

To identify parameters with the greatest diagnostic potential, we performed unsupervised Principal Component Analysis (PCA) (Abdi, 2010). PCA projects interdependent correlated variables onto orthogonal Principal Components (PCs) ranked by degree of variance explained. Variable loadings indicate the relative influence of the six original measurements on an individual PC, with higher absolute values representing a stronger contribution. In Fig. 4c, bulk ADAM-10 enzymatic activity contributes the highest to PC1 with a loading of 0.62,

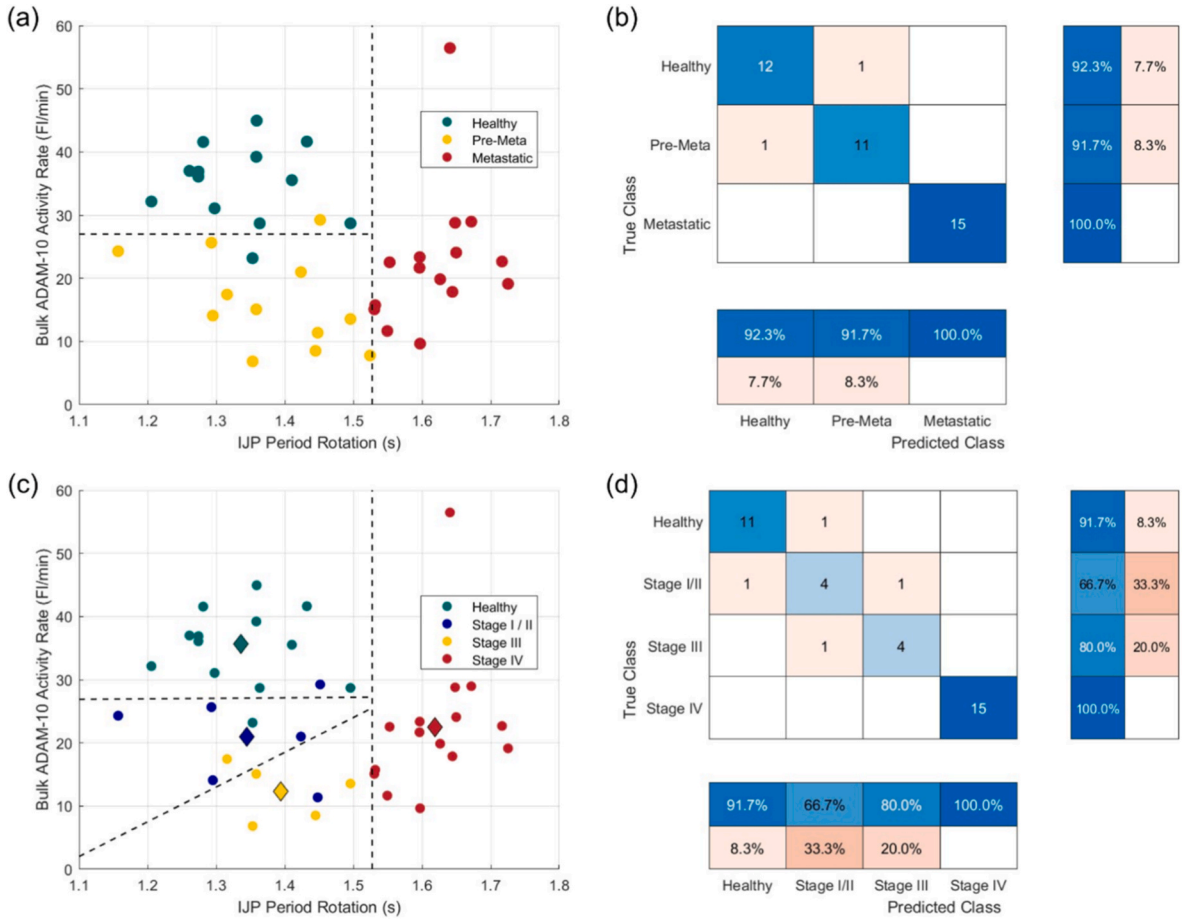

Fig. 5. Bimodal analysis of bulk ADAM-10 enzymatic activity rate and Immuno-Janus Particle period enables accurate classification of metastatic potential and colorectal cancer stage. (a) Scatter plot of bulk ADAM-10 activity (y-axis) versus IJP period (x-axis) for individual patients. Dashed lines represent decision boundaries separating healthy, pre-metastatic, and metastatic groups. (b) Confusion matrix for linear discrimination classification showing true labels (rows) versus predicated labels (columns). Group precision and recall are displayed in the right-most and bottom panels, respectively. (c) Scatterplot with refined classification, dividing pre-metastatic samples into Stage I/II and Stage III cancer. Diamonds represent population averages for their respective group and circles represent individual patient data. One pre-metastatic sample was excluded as it was not assigned a stage. (d) Confusion matrix showing classification performance for stage-wise analysis using bimodal input variables.

while IJP period is highest for PC2 (0.71). These two leading components contribute 47.7% and 24.1% variance respectively, explaining 71.8% of system variance (Fig. 4d), indicating a bimodal ADAM-10 quantification is likely diagnostically sufficient for CRC stage classification. For additional diagnostic potency, PC3 (mean particle diameter, loading = 0.86) and PC4 (protein concentration, loading = 0.95) can be incorporated, contributing an additional 13.6% and 7.4% of system variance, respectively (Fig. 4c and d). Importantly, this small change in EV diameter from an orthogonal NTA characterization confirms that the change in IJP period is due to a change in ADAM-10+ EV concentration. Our findings from principal component analysis suggest that leveraging ADAM-10 activity and IJP period would provide a minimalistic, diagnostically accurate screening platform for cancer staging. We will explore this relationship and uncover trends in the next section.

2.6. *Colorectal cancer progression is reflected in ADAM-10+ vesicles and bulk activity*

We explored the diagnostic potential of combined orthogonal IJP period and bulk ADAM-10 activity for colorectal cancer progression. In Fig. 5a, healthy patients exhibit elevated bulk activity and quicker IJP rotation, whereas pre-metastatic samples show a marginally increased IJP period but a significantly reduced bulk activity. Metastatic samples are characterized by significantly larger IJP blinking periods and slightly higher bulk activity, except metastatic patient M7, who shows unusually high ADAM-10 activity despite having a characteristic IJP period. The orthogonal separation between activity and affinity for premetastatic and metastatic samples in Fig. 5a is striking and underscores the need for a bimodal assay for accurate metastatic assessment.

Applying simple thresholding values, the IJP period >1.53 s perfectly isolates the metastatic samples. Pairing faster periods with a bulk activity of 27 FI/min defines the pre-metastatic and healthy cohort boundaries, allowing for the implementation of a linear discrimination classifier in Fig. 5b. The precision/recall values achieved are 100% for metastatic, 91.7% for pre-metastatic, and 92.3% for healthy samples across 40 total patients. Misclassifications were limited to one sample in both non-metastatic groups, granting an overall 95% accuracy. As a pilot study, these results justify further investigation into the interdependence of ADAM-10 activity and ADAM-10+ EV content as bimodal disease progression markers. Surprisingly, the fraction of active ADAM-10+ plasma EVs is lower in early premetastatic patients than in healthy samples, while the concentration of both active and inactive ADAM-10+ EVs increases for post-metastatic samples.

To explore stage resolution of this capture and activity-based study,

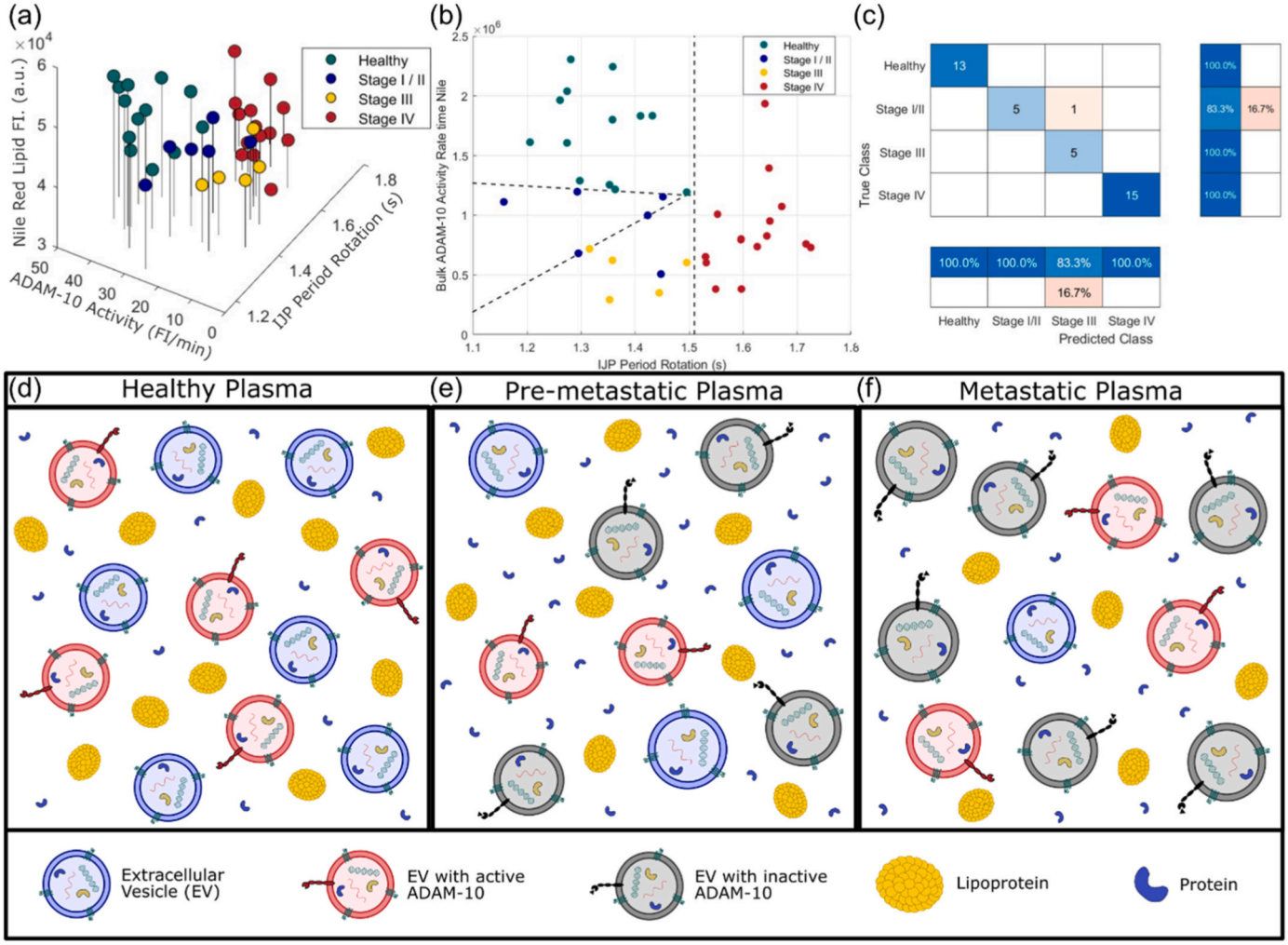

Fig. 6. Trimodal analysis of lipid content, enzymatic activity, and IJP period enhances diagnostic staging of colorectal cancer, and schematic summary plasma profiles. (a) Ternary plot of IJP period, bulk ADAM-10 activity, and Nile Red lipid fluorescence across healthy, Stage I/II, Stage III, and Stage IV cohorts. (b) Two-dimensional projection showing IJP period versus the multiplication of ADAM-10 activity and lipid content. Dashed lines indicate classification thresholds. (c) Confusion matrix showing 97.4% overall accuracy of stage-wise performance using trimodal analysis. (d-f) Schematics of plasma composition across disease progression, showing an increase in proteins, decrease in lipoproteins, and a reconfiguration of ADAM-10 to inactive, yet more abundant forms. (For interpretation of the references to color in this figure legend, the reader is referred to the Web version of this article.)

we partitioned the pre-metastatic cohort into Stage I/II cancer, and Stage III cancer at the time of diagnosis (Fig. 5c). Stage I was combined with Stage II due to sample quantity, and one un-staged pre-metastatic sample was omitted. The Diamond symbols in Fig. 5c represent the group stage-wise behavior. It shows that Stage I/II experience an early reduction in enzymatic activity, and a slight increase in ADAM-10+ EV quantity. Stage III continues this same general trend. Stage IV, metastatic samples demonstrate an increase in activity and the largest adjacent inter-group IJP period increase, indicating the most drastic shift in vesicle's conformational volume upon the initial metastasis of the tumor. Patients of the same stage have similar IJP periods and enzymatic activity, resulting in a tight clustering of the group behavior. Subsequently, a few misclassifications occur between adjacent stages (i.e. no healthy sample was identified as stage III/IV).

Stage-based identification in Fig. 5d achieved a diagnostic accuracy of 89.7%, with all misclassifications occurring in early-stage samples, adjacent or within Stage I/II. This high staging resolution underscores the merit of incorporating activity- and expression-based diagnostics, accurately pinpointing stage and allowing for earlier, more robust cancer interventions.

2.7. ADAM-10 enzymatic disparities among cells, cell culture EVs, and plasma EVs

Healthy patient plasma exhibits the highest ADAM-10 activity despite having the fewest ADAM-10+ EVs as defined by the IJP period (Fig. 5a and c), a trend opposite to that observed in cell-culture assays (Supporting Fig. 4d) where metastatic cell lines exhibit elevated activity. This discrepancy likely reflects differences in therapeutic intervention, or culture system tumor physiology. In solid tumor environments, EV transport through the unvascularized extracellular matrix is innately limited, a behavior not captured in monolayer cultures or more advanced organoid models. Moreover, transport resistance is selectively more severe for EVs with active ADAM-10, given their function to bind to cell-surface receptors and perform initiation cleavage events on the order of hours (Fig. 2). Hence, active ADAM-10 EVs are enriched locally within the tumor microenvironment, while their dissipation into circulation is diminished relative to inactive EVs.

Moreover, regulatory mechanisms not captured in cell culture may further limit plasma ADAM-10 activity in cancer patients. Membrane-bound ADAM-10 enhances cancer proliferation through erbB ligands such as EGF (Moss et al., 2007), but therapeutic inhibition of the EGFR signaling elevates ADAM-10 pro-domain levels and enhances ADAM-10 self-dimerization collectively suppressing ADAM-10 activity (Deng et al., 2014; Moss et al., 2007; Wetzel et al., 2017). Reduced cholesterol in unvascularized tumors due to low nutrient transport may further impair ADAM-10 function, which mirrors regulatory pathways described for ADAM-17; the metalloproteinase's proximity to lipid rafts and cholesterol-dependent interactions modulate shedding efficiency (Tellier et al., 2006). We observe a correlated level change in lipoproteins that transport cholesterol (Fig. 6). We suggest the synergistic factors of transport limitation, receptor engagement, metabolic inhibition, and lipid dysregulation, which result in diminished production and circulation of active ADAM-10 EVs in cancer patients, especially the pre-metastatic niche.

A decrease in plasma EV ADAM-10 activity has been previously noted in metastatic patients(Tugutova et al., 2019), aligning with other reports of disease-associated dysregulation of metalloproteinase activity (Aljohmani et al., 2022; Ebsen et al., 2013; Moss et al., 2007; Wetzel et al., 2017). These studies, along with our findings, support a spatial model of ADAM-10 regulation. Locally elevated enzymatic activity at the tumor site facilitates ECM remodeling and invasion, whereas distant EV-associated activity is reduced by regulatory constraints including ECM density, lipid raft disruption, and pro-domain mediated inhibition. This framework reconciles the paradox between elevated ADAM-10 activity in tumors and cell culture, with a reduced EV-normalized activity observed in pre-metastatic plasma. Additionally, in vascularized metastatic tumors, increased EV release, enhanced vascular access, and the more permeable ECM would lead to the observed modest recovery of ADAM-10 activity per EV.

2.8. Trends in ADAM-10+ EVs and composition across colorectal cancer progression

To improve upon the separation of disease cohorts, we posit the merits of a third diagnostic modality, such as NTA size distribution, which contributed to the highest system variance following enzymatic activity and IJP period (Fig. 3c and d). Although metastatic samples display a general positive correlation between particle size and disease state (Fig. 4c), the high intragroup size variability severely constrains diagnostic resolution. Because particle size does not statistically determine cancerous diseases from healthy groups, we sought a modality that consistently downregulates during tumor development. Nile Red lipid signal decreases significantly alongside ADAM-10 activity (Fig. 4b), making it a viable option for analysis.

Fig. 6a presents a ternary analysis merging IJP period, bulk ADAM-10 activity, and Nile Red lipid fluorescence. The three-dimensional plot of the four groups reveals distinct clustering, offering improved separation compared to IJP rotation and ADAM-10 activity alone enhanced separation. Due to the inclusion of the Nile Red reported lipid content, a statistically significant decrease in signal second only to enzymatic rate is achieved (Fig. 4b). Notably, both lipid content and vesicle concentration decline from healthy to metastatic stages, suggesting a reduction in lipid-rich lipoproteins (Jiang et al., 2006; Kokoglu et al., 1994; Kritchevsky et al., 1991; van Duijnhoven et al., 2011) or exosomal subtypes of EVs. This association helps reconcile the discrepancy of higher ADAM-10+ EVs concentration but fewer total particles.

A simplified two-dimensional plot (Fig. 6b) demonstrates the power of this three-variable analysis. By multiplying the ADAM-10 activity and the Nile Red lipid content, we achieved a clear separation of the healthy and pre-metastatic samples, enabling an accurate disease staging assessment. The selected delineations achieved 100% accuracy for both cancer presence and metastatic potential, and an impressive 97.4% accuracy for stage determination. Only a single stage I/II patient was misclassified as stage III (Fig. 6c), underscoring the likelihood that large-scale clinical application will inevitably blur the sharp thresholds. For a more robust statistical analysis of the cohort separations, Linear Discriminant Analysis (LDA) was conducted to generate decision-driven separations based on mean patient expression levels. This still achieved an excellent 92.5% metastatic staging accuracy (Supporting Fig. 3d–f), more aligned with clinical translatability expectations.

While Nile Red lipid content enhanced our diagnostic separation, lipid and enzymatic analyses are incapable of solely achieving the high discriminatory power (72.1% overall accuracy) without the IJP EV-bound ADAM-10 signal, suggesting why the combination had not been employed previously (Supporting Fig. 3a–c). Regardless, the strong stage-dependent trends discovered across this trimodal analysis in the 43-patient pilot study hold significant translational potential. Combining the stage-wise diagnosis in this work with the disease type screening from our previous work (Kumar et al., 2025) would allow us to identify cancer location and progression in <60 min with a single blood draw.

To visually contextualize the trends found in this multimodal analysis of 43 patients spanning three disease states and six diagnostic parameters, we constructed simplified schematic overviews of plasma composition across metastatic progression (Fig. 6d–f). Relative to healthy expression levels, diseased plasma contains reduced lipoproteins, increased soluble proteins, and a shift towards inactive EV-bound ADAM-10, leading to lengthened IJP periods without a reciprocal increase in bulk enzymatic activity assay. Tumor-associated EV release increases in late-stage disease (Bebelman et al., 2021; Surman et al., 2017; Xu et al., 2018), with higher ADAM-10+ EV concentration

coinciding with a substantial reduction in lipid-rich particles. Reduced EV concentration in pre-metastatic samples may result from tumor therapy or tumor-induced metabolic suppression of non-tumor cells, further enhancing the proportional contribution of tumor-derived EVs.

These compositional shift suggests a redistribution of ADAM-10+ EVs to larger vesicles such as *lEVs* or microvesicles. Prior studies report ADAM-10 enrichment in the small EV fractions of (100K ultracentrifugation pellets) (Kowal et al., 2016), yet large EVs (100-1000 nm) such as microvesicles and ectosomes are increasingly abundant in cancer plasmas (glioblastoma, non-small-cell lung carcinoma, multiple myeloma) and carry pertinent established markers (e.g. MUC1, CEA, CA19-9) (Surman et al., 2017). Our observations of larger particles and slower IJP blinking rates in metastatic plasma support this transition. Expanding multimodal assays to incorporate additional modalities for larger EVs, such as our recent Surface Acoustic Wave sensor platform (Cheng et al., 2025) would discern the various factors regarding ADAM-10 carriers through disease progression. Ultimately, a multimodal affinity-activity assay on colocalized biomarkers analysis serves as the most comprehensive, minimally invasive, screening assay for cancer detection and staging. To improve clinical applicability, low-dimensional Principal Component analysis enhanced by advanced machine learning for large-library activity/affinity assays across a breadth of diseases.

3. Conclusions

This work establishes a bimodal activity/affinity assay for ADAM-10+ EVs as a promising platform for assessing the metastatic status in colorectal cancer. We demonstrate that intact plasma (EVs) carrying the enzymatically active forms of ADAM-10, and that these vesicles account for the majority of the signal observed in bulk plasma enzymatic assays. By analyzing progressively metastatic, androgen-insensitive prostate cancer cell lines (LNCaP, 22Rv1, DU145, and PC3), we observe a general increase in ADAM-10 enzymatic rate dependent on the EV concentration.

Multimodal profiling combined with PCA revealed that IJP rotation period (a surrogate for ADAM-10+ EV abundance) combined with bulk ADAM-10 activity explained a majority of the diagnostic variance. The bimodal screening enabled a 95% accurate metastatic potential identification, while implementing lipidomics as a third modality achieved 100% accuracy for cancer identification and metastatic potential, and 97.4% accuracy for stage classification. These results highlight the importance of integrating multiple affinity/activity based analytical methods into a unified framework for orthogonal EV liquid biopsies.

Beyond diagnostic performance, our findings ascertained mechanistic insights into ADAM-10 regulation in cancer. While ADAM-10+ EVs are plentiful in healthy human plasma, we found that these species become largely reduced in the plasma of early-stage CRC patients. We hypothesize that these non-linear responses arise from the previously proposed ECM retention effect (in Section 2.7) along with a transient humoral autoimmune response against ADAM-10. CRC cohorts exhibit maximal anti-ADAM-10 autoimmune response in pre-metastatic Stages II and III, potentially leading to reduction of ADAM-10+ EVs in early stages of disease (Alvarez-Fernandez et al., 2016). Moreover, it has been found that under inflammatory conditions, healthy expression of ADAM-10 in somatic cells may be reduced or disrupted (Sakamoto et al., 2021). Taking together with our findings, these reports support a complex, non-monotonic relationship between ADAM-10 and CRC that motivates multimodal assays to achieve high selectivity and specificity for prognosis, staging, and therapeutic monitoring. While these mechanisms remain speculative, we are partnering with clinical collaborators to test them in vivo and delineate the coupled dynamics of ADAM-10 and EVs across CRC progression. These findings underscore ADAM-10 based multimodal EV assays as highly selective tools for prognosis, disease staging, and therapeutic monitoring. Augmentation of established disease markers or MPs, affinity/activity multiplexing, and machine learning analysis of a large library of assays could bolster this platform into a scalable screening platform for a wide breadth of cancers, in addition to other diseases.

4. Experimental section

4.1. Clinical patient plasma pre-processing

The CRC patient and healthy cohort sample population was established from the biosample matrix catalog provided by Precision for Medicine with a filter focusing on individuals of non-Hispanic white ethnic background ranging from 48 to 82 years of age with roughly equal split between male (n = 22) and female (n = 21) individuals to minimize variance caused by demographic factors. All samples were K2 EDTA plasma samples stored at −80 °C after sample draw. Further demographic information can be found in Table 1.

Operations utilizing patient plasma samples were performed in a BSL-2 biohazard hood. Raw plasma samples were diluted by 10X in 1X DPBS (Gibco, Cat. 14200-075) upon receipt before filtering through MiniSart High Flow 0.22-μm (Sartorius, Cat. 16541-K) syringe filters. Samples were aliquoted and stored in −80 °C until needed.

4.2. Immuno-Janus Particle fabrication

Immuno-Janus Particles were synthesized in-house. 200 μL of 1.0 μm FluoSpheres™ Polystyrene Microspheres (Thermo Fisher, Cat. F13081/F13083) are added to 10 mL of 70% v/v isopropyl alcohol (VWR, Cat. BDH7999-4). An Electro-Technic Products Inc Model BD-20 High Frequency Generator plasma treated a plain microscope slide (VWR, Cat. 48300-026) for 15 s before adding 1 mL of dilute FluoSpheres™ solution on top. The organic solution was allowed to evaporate overnight, leaving a monolayer of dry plain beads. Eight slides were inserted into an AIRCO Temescal FC 1800 electron beam vacuum deposition/thin-film coater system, and coated with 2 nm titanium, followed by 28 nm gold at a deposition rate between 0.5 and 1.0 Å/s. Slides were unaffixed from the PVD machine, and snapped in half longways before being placed in a 1% v/v Tween-20 (Sigma-Aldrich, Cat. P9416-50 ML) in DI H_2O solution. This solution was bath sonicated for 10 min in an ultrasonic cleaner (Bransonic®, Model 5510R-DTH) to dislodge particles from the slide. The slides were removed from the solution and the remaining solution was filtered twice with a 5 μm disk filters (Cytiva Whataman™ Puradisc™, Cat. 10463533) to remove aggregates, glass shards, and impurities. The permeate was centrifuged on a AccuSpin Micro 17 (Fisher, Cat. 13100675) at 6000g for 4 min before removing the supernatant and concentrating the beads into a volume of about 1 mL, resulting in a final IJP concentration of 1 $\times 10^7$ particles/mL. The solution was stored in a 4 °C fridge until antibody functionalization for experiments.

4.3. Immuno-Janus Particle antibody functionalization onto gold hemisphere

Gold Conjugation Kit (Abcam, Cat. ab154873) was used to functionalize anti-ADAM-10 monoclonal antibody (Proteintech, Cat. 66620-1-Ig, Lot. 10007605) onto the IJPs' golden hemisphere. 20 μL of the 1500 μg/mL antibody was combined with 84 μL of Abcam Gold conjugation buffer. 90 μL of this solution was added to 200 μL prepared IJP solution and allowed to incubate for 15 min on a shaker (Scilogex, Model MX-M) at 1000 rpm. Abcam Gold conjugation quencher (10 μL) was added to this solution and continued to shake on the shaker for another 15 min. The solution was centrifuged in a Fisher AccuSpin Micro 17 at 6000g for 4 min and washed with 1:400 Tween-20 (Sigma-aldrich P9416-50 ML): DI H20 one time, followed by two washes with 10 times diluted Dulbecco's Phosphate Buffered Saline (VWR, Catalog no. 02-0119-1000) in DI H_2O to remove any non-bound antibodies. Functionalized IJPs were resuspended in 50 μL of 10x diluted PBS.

4.4. Imaging the Immuno-Janus Particles

The prepared IJP solution was incubated in a 2:1 ratio with each plasma sample in a 0.2 mL PCR tube (Axygen, Ref PCR-02-C). These PCR tubes were placed on a shaker (Scilogex MX-M) at 750 rpm for 1 h before imaging. A custom-made apparatus was constructed to image samples effectively. Three cover micro covers (VWR, Catalog no. 48366-089) are stacked and affixed on each side of a microscope slide (VWR, Catalog no. 48300-026). A 2 μL droplet of IJP-sample solution is placed in the middle of the slide, where another microscope cover is placed on top, creating a capillary bridge that suspends the droplet in place. This custom apparatus is placed on an Olympus IX-71 inverted microscope with an Olympus Optical Co., LTD 100 W High Pressure Mercury Burner (Model no. BH2-RFL-T3, no. 2308002) supplying the fluorescent signal. The 10$\times$ objective was focused at 200 μm above the glass slide for recording. Three technical replicates were recorded using a Basler ace 2 R (Basler, Catalog no. a2A1920-160ucPRO) camera at a frame rate of 10 Hz at a duration of 120 s per replicate.

4.5. Nanoparticle tracking analysis procedure

NTA measurements were performed using NanoSight NS300 (Malvern, UK) (Harper Cancer Research Institute, University of Notre Dame, Notre Dame, IN) per manufacturer protocol (NanoSight NS300 User-Manual, MAN0541-01-EN-00, 2017). Each sample was measured via a three-point serial dilution in 1X DPBS to ensure reliability. Camera settings are Capture Gain = 8, Camera Level = 10, Focus = 450, Process Gain = 10, and Detection Threshold = 3. Reported concentrations are scaled to original sample volumes.

4.6. ADAM-10 bulk activity assay procedure

ADAM-10-specific activity substrate sequence (N to C) consists of a DABCYL quencher, a specific peptide sequence (PRAEALKGGK) (Chen et al., 2021), and a 5-FAM fluorophore. Custom peptide sequence produced via Biomatik Corporation Custom Peptide Synthesis at 90.91% purity and MW 1935.79 Da (Biomatik, Lots. GT91736-SP230343, P240218-LL1143224). Lyophilized peptide substrate is resuspended in 1X DPBS and solubilized via bath sonication for 1 min (QSonica, Model Q125 & CL-18). Excitation and emission frequencies for peptide fluorophore were optimized at 485-nm and 525-nm, respectively (Supporting Fig. 4c). Fluorescent intensities were measured using Tecan Infinite® 200 PRO (Tecan Trading AG, Mannedorf, Switzerland) plate reader. Fluorescent growth rate at limit of detection (LoD) was determined through calibration performed using recombinant human ADAM-10 (rhADAM-10) (R&D Systems, Cat. 936-AD-020). The calibration curve is shown in Supporting Fig.b.

For Michaelis-Menton normalization testing, eight dilutions of ADAM-10 substrate (5 - 1000 μM) were formulated and tested against three dilutions (1X, 2D, 4D) of filtered healthy human plasma and filtered healthy human dermal cell cultured media. Fold dilution will be denoted by the form of yD where y is any positive number. This notation describes a fold dilution of a given sample where the ratio of final volume to initial volume is y:1. Alternatively, fold concentrations will be denoted by the form of zX where z is any positive number. This notation describes a fold concentration of a given sample where the ratio of initial volume to final volume is z:1. For cell culture & clinical plasma samples, ADAM-10 substrate concentration is 200-μM and samples are tested at 1X concentration and 2D dilution. Each reaction consists of 50-μL substrate and 50-μL sample. Samples were kinetically measured for 120 min at 10-min intervals. Fluorescent growth rates were calculated by calculating slopes for fluorescent intensities measured from 20 to 60 min after reaction initiation.

4.7. Healthy human plasma and dermal cell cultured media fractioning and EV lysis

Diluted and 0.22-μm syringe filtered plasma and cell culture samples were spin filtered using NanoSep 300K Omega (Pall, Cat. OD300C34) spin filters at 2.5kxg for 20 min. Flowthrough was reserved and the retentates were further washed with 1X DPBS. Fractions of the retentate are incubated in 0.10 wt% final concentration of Triton X-100 (Thermo Fisher, Cat. J62289.AP, Lot. M24J506) for 5 min on an orbital shaker at room temperature. Control fractions were taken and incubated simultaneously in equivalent volumes of 1X DPBS. Incubated samples were filtered using SpinX UF500 10k MWCO PES Filter (Corning, Cat. 431478, Lot. 16323005) at 12kxg for 10 min and washed using 1X DPBS. All reserved fractions were reconstituted to original sample volumes.

4.8. Total CD63 & ADAM-10 ELISA for healthy human plasma fractions

All samples were evaluated using Human CD63 ELISA Kit (AbCam, Cat. ab275099, Lot. 2101053719) and Human ADAM-10 ELISA Kit (AbCam, Cat. ab309315, Lot. 2101052036) per manufacturer protocols. Endpoint fluorescent intensities were measured using Tecan Infinite® 200 PRO (Tecan Trading AG, Mannedorf, Switzerland) plate reader. Calibration curves for CD63 and ADAM-10 assays are shown in Supporting Fig. 1c and b, respectively.

4.9. Prostate cancer cell cultured media and EV collection

PC3, DU145, 22Rv1, and LNCaP prostate cancer cell lines were maintained in 10 cm culture dishes in RPMI-1640 medium (Gibco) supplemented with 10% fetal bovine serum (FBS; Gibco). Upon reaching confluence, cells were washed twice with phosphate-buffered saline (PBS; 1 $\times$) to remove residual serum components. The culture medium was then replaced with 10 mL of RPMI-1640 containing 10% exosome-depleted FBS (Gibco), and cells were incubated for 48 h. Conditioned media were subsequently collected for exosome isolation.

4.10. Bradford total protein assay procedure

Total protein assay was designed using 150-μL Bradford Reagent (Sigma Millipore, Cat. B6916-500 ML; Lot. SLCN3585) applied to 5-μL of each target sample. Samples are incubated for 30 min on an orbital shaker at room temperature. Absorbance intensities at 595-nm were measured using Tecan Infinite® 200 PRO (Tecan Trading AG, Mannedorf, Switzerland) plate reader. Protein standards (1 – 2250 μg/mL) were formulated from step dilutions of Bovine Serum Albumin 30% in DPBS (Sigma Millipore, Cat. A9576-50 mL, Lot. SLCL8813). Calibration curve for Bradford total protein assay is shown in Supporting Fig. 5c.

4.11. Nile Red total lipid assay procedure

Lyophilized Nile Red (Thermo Fisher, Cat. N1142, Lot. 2916406) is reconstituted to 1-mg/mL in 1X DPBS. Samples are incubated at 20-μg/mL final concentration Nile Red for 30 min before imaging. Excitation and emission frequencies for Nile Red assay were optimized at 555-nm and 635-nm, respectively (Supporting Fig. 5b). Fluorescent intensities were measured using Tecan Infinite® 200 PRO (Tecan Trading AG, Mannedorf, Switzerland) plate reader. Calibration curve for Nile Red total lipid assay is shown in Supporting Fig. 5a.

4.12. Unsupervised learning procedure for principal component analysis

Group expressions were compiled for all 43 patients whose samples were analyzed in this study. An average and standard deviation was calculated for the healthy group for each of the six studied parameters. All samples subtracted the average healthy expression and were then divided by the healthy standard deviation to determine a z-score.

MATLAB's PCA function was used to calculate and store the principal component coefficient matrix, variable weights and loadings, as well as the variance explained by said parameter. These values were used to determine parameters contributing most significantly towards the system variance and the degree attributed.

4.13. Statistical analysis

The data presented here is expressed as the mean and standard deviation or standard error of the mean as calculated using Excel, Python, or GraphPad Prism 8 software functions. Errors are propagated through formulas using standard propagation of uncertainties techniques.

Ethics approval and consent to participate

We received colorectal cancer and healthy group plasma samples from Precision for Medicine, and unlabeled and randomized immediately upon arrival. An approved IRB protocol is already in place at Precision for Medicine for the collection of plasma samples from patients. Precision for Medicine works with regulatory authorities and accrediting organizations around the world to ensure that the sample collection process and protocol follow the latest FDA, EMA, and MHRA guidelines. All procedures performed in studies involving human participants were conducted in accordance with the ethical standards of the University of Notre Dame.

Consent for publication

Not applicable.

Availability of data and materials

The datasets used and/or analyzed during the current study are available from the corresponding author on reasonable request.

Funding

H.C.C and S.S acknowledge the partial support from the Common Fund through the Office of Strategic Coordination/Office of the NIH Director under 4UH3CA241684-01 and from the NIH, 1R21AI180713-01A1. Xin Lu acknowledges the support from NIH grants R01CA248033, R01CA280097, and R01CA297220.

CRediT authorship contribution statement

Tiger Haoran Shi: Conceptualization, Data curation, Formal analysis, Investigation, Methodology, Validation, Visualization, Writing – original draft, Writing – review & editing. **John Alex Sinclair:** Conceptualization, Data curation, Formal analysis, Investigation, Methodology, Validation, Visualization, Writing – original draft, Writing – review & editing. **Youwen Zhang:** Formal analysis, Investigation, Methodology. **Xuemin Lu:** Resources, Writing – review & editing. **Sonu Kumar:** Conceptualization, Formal analysis, Methodology. **Xin Lu:** Funding acquisition, Resources, Writing – review & editing. **Satyajyoti Senapati:** Conceptualization, Formal analysis, Funding acquisition, Methodology, Resources, Supervision, Visualization, Writing – review & editing. **Hsueh-Chia Chang:** Conceptualization, Formal analysis, Funding acquisition, Methodology, Project administration, Resources, Supervision, Visualization, Writing – review & editing.

Declaration of competing interest

The authors declare the following financial interests/personal relationships which may be considered as potential competing interests: Hsueh-Chia Chang, Sonu Kumar, Satyajyoti Senapati, and John Alex Sinclair has patent (Application No. 19/153,414) pending to University of Notre Dame du Lac. If there are other authors, they declare that they have no known competing financial interests or personal relationships that could have appeared to influence the work reported in this paper.

Acknowledgments

We thank Gaeun Kim of Prof. Yichun Wang's lab, Department of Chemical and Biomolecular Engineering, University of Notre Dame, for providing the patient-derived healthy human dermal cell culture media for the initial experiments. We thank the Tissue Bank at the Harper Cancer Research Institute (HCRI), University of Notre Dame, for use of the NanoSight NS300 for nanoparticle tracking analysis.

Appendix A. Supplementary data

Supplementary data to this article can be found online at https://doi.org/10.1016/j.bios.2026.118517.

Data availability

Data will be made available on request.

References

Abdi, H.W.L., 2010. Principal component analysis. Wires Comput. Stat. 2 (4), 433–459. https://doi.org/10.1002/wics.101.

Abusamra, A.J., Zhong, Z., Zheng, X., Li, M., Ichim, T.E., Chin, J.L., Min, W.P., 2005. Tumor exosomes expressing Fas ligand mediate CD8+ T-cell apoptosis. Blood Cells Mol. Dis. 35 (2), 169–173. https://doi.org/10.1016/j.bcmd.2005.07.001.

Aljohmani, A., Opitz, B., Bischoff, M., Yildiz, D., 2022. Pseudomonas aeruginosa triggered exosomal release of ADAM10 mediates proteolytic cleavage in trans. Int. J. Mol. Sci. 23 (3). https://doi.org/10.3390/ijms23031259.

Alvarez-Fernandez, S.M., Barbariga, M., Cannizzaro, L., Cannistraci, C.V., Hurley, L., Zanardi, A., Conti, A., Sanvito, F., Innocenzi, A., Pecorelli, N., Braga, M., Alessio, M., 2016. Serological immune response against ADAM10 pro-domain is associated with favourable prognosis in stage III colorectal cancer patients. Oncotarget 7 (48), 80059–80076. https://doi.org/10.18632/oncotarget.11181.

Bebelman, M.P., Janssen, E., Pegtel, D.M., Crudden, C., 2021. The forces driving cancer extracellular vesicle secretion. Neoplasia 23 (1), 149–157. https://doi.org/10.1016/j.neo.2020.11.011.

Cai, C., Zhang, M., Liu, L., Zhang, H., Guo, Y., Lan, T., Xu, Y., Ma, P., Li, S., 2022. ADAM10-cleaved ephrin-A5 contributes to prostate cancer metastasis. Cell Death Dis. 13 (5), 453. https://doi.org/10.1038/s41419-022-04893-8.

Cavallaro, S., Horak, J., Haag, P., Gupta, D., Stiller, C., Sahu, S.S., Gorgens, A., Gatty, H. K., Viktorsson, K., El Andaloussi, S., Lewensohn, R., Karlstrom, A.E., Linnros, J., Dev, A., 2019. Label-Free surface protein profiling of extracellular vesicles by an electrokinetic sensor. ACS Sens. 4 (5), 1399–1408. https://doi.org/10.1021/acssensors.9b00418.

Chen, X., Gole, J., Gore, A., He, Q., Lu, M., Min, J., Yuan, Z., Yang, X., Jiang, Y., Zhang, T., Suo, C., Li, X., Cheng, L., Zhang, Z., Niu, H., Li, Z., Xie, Z., Shi, H., Zhang, X., Fan, M., Wang, X., Yang, Y., Dang, J., McConnell, C., Zhang, J., Wang, J., Yu, S., Ye, W., Gao, Y., Zhang, K., Liu, R., Jin, L., 2020. Non-invasive early detection of cancer four years before conventional diagnosis using a blood test. Nat. Commun. 11 (1), 3475. https://doi.org/10.1038/s41467-020-17316-z.

Chen, X., Zhang, Y., Guan, X., 2021. Simultaneous detection of multiple proteases using a non-array nanopore platform. Nanoscale 13 (32), 13658–13664. https://doi.org/10.1039/d1nr04085e.

Cheng, C.H., Yatsuda, H., Liu, S.H., Tsai, W.N., Cheng, T.S., Chen, S.Y., Huang, C.F., Chang, H.C., Kondoh, J., 2025. An approach for measuring extracellular vesicle size using the attenuation-velocity change ratio of SH-SAW biosensors. Anal. Chem. https://doi.org/10.1021/acs.analchem.5c01881.

Clark, I.M., Swingler, T.E., Sampieri, C.L., Edwards, D.R., 2008. The regulation of matrix metalloproteinases and their inhibitors. Int. J. Biochem. Cell Biol. 40 (6-7), 1362–1378. https://doi.org/10.1016/j.biocel.2007.12.006.

Costa-Silva, B., Aiello, N.M., Ocean, A.J., Singh, S., Zhang, H., Thakur, B.K., Becker, A., Hoshino, A., Mark, M.T., Molina, H., Xiang, J., Zhang, T., Theilen, T.M., Garcia-Santos, G., Williams, C., Ararso, Y., Huang, Y., Rodrigues, G., Shen, T.L., Labori, K.J., Lothe, I.M., Kure, E.H., Hernandez, J., Doussot, A., Ebbesen, S.H., Grandgenett, P.M., Hollingsworth, M.A., Jain, M., Mallya, K., Batra, S.K., Jarnagin, W.R., Schwartz, R. E., Matei, I., Peinado, H., Stanger, B.Z., Bromberg, J., Lyden, D., 2015. Pancreatic cancer exosomes initiate pre-metastatic niche formation in the liver. Nat. Cell Biol. 17 (6), 816–826. https://doi.org/10.1038/ncb3169.

Cox, T.R., 2021. The matrix in cancer. Nat. Rev. Cancer 21 (4), 217–238. https://doi.org/10.1038/s41568-020-00329-7.

Crosby, D., Bhatia, S., Brindle, K.M., Coussens, L.M., Dive, C., Emberton, M., Esener, S., Fitzgerald, R.C., Gambhir, S.S., Kuhn, P., Rebbeck, T.R., Balasubramanian, S., 2022.

Early detection of cancer. Science 375 (6586), eaay9040. https://doi.org/10.1126/science.aay9040.
Dempsey, P.J., 2017. Role of ADAM10 in intestinal crypt homeostasis and tumorigenesis. Biochim. Biophys. Acta Mol. Cell Res. 1864 (11 Pt B), 2228–2239. https://doi.org/10.1016/j.bbamcr.2017.07.011.
Deng, W., Cho, S., Su, P.C., Berger, B.W., Li, R., 2014. Membrane-enabled dimerization of the intrinsically disordered cytoplasmic domain of ADAM10. Proc. Natl. Acad. Sci. U. S. A. 111 (45), 15987–15992. https://doi.org/10.1073/pnas.1409354111.
Ebsen, H., Schroder, A., Kabelitz, D., Janssen, O., 2013. Differential surface expression of ADAM10 and ADAM17 on human T lymphocytes and tumor cells. PLoS One 8 (10), e76853. https://doi.org/10.1371/journal.pone.0076853.
Elsworthy, R.J., Hill, E.J., Dunleavy, C., Aldred, S., 2022. The role of ADAM10 in astrocytes: implications for Alzheimer's disease. Front. Aging Neurosci. 14, 1056507. https://doi.org/10.3389/fnagi.2022.1056507.
Fabbri, M., Paone, A., Calore, F., Galli, R., Gaudio, E., Santhanam, R., Lovat, F., Fadda, P., Mao, C., Nuovo, G.J., Zanesi, N., Crawford, M., Ozer, G.H., Wernicke, D., Alder, H., Caligiuri, M.A., Nana-Sinkam, P., Perrotti, D., Croce, C.M., 2012. MicroRNAs bind to toll-like receptors to induce prometastatic inflammatory response. Proc. Natl. Acad. Sci. U. S. A. 109 (31), E2110–E2116. https://doi.org/10.1073/pnas.1209414109.
Fang, H., Peng, B., Ong, S.Y., Wu, Q., Li, L., Yao, S.Q., 2021. Recent advances in activity-based probes (ABPs) and affinity-based probes (AfBPs) for profiling of enzymes. Chem. Sci. 12 (24), 8288–8310. https://doi.org/10.1039/d1sc01359a.
Gao, R., Li, X., 2023. Extracellular vesicles and pathological cardiac hypertrophy. Adv. Exp. Med. Biol. 1418, 17–31. https://doi.org/10.1007/978-981-99-1443-2_2.
Gavert, N., Sheffer, M., Raveh, S., Spaderna, S., Shtutman, M., Brabletz, T., Barany, F., Paty, P., Notterman, D., Domany, E., Ben-Ze'ev, A., 2007. Expression of L1-CAM and ADAM10 in human colon cancer cells induces metastasis. Cancer Res. 67 (16), 7703–7712. https://doi.org/10.1158/0008-5472.CAN-07-0991.
Guan, X., 2015. Cancer metastases: challenges and opportunities. Acta Pharm. Sin. B 5 (5), 402–418. https://doi.org/10.1016/j.apsb.2015.07.005.
Hakulinen, J., Sankkila, L., Sugiyama, N., Lehti, K., Keski-Oja, J., 2008. Secretion of active membrane type 1 matrix metalloproteinase (MMP-14) into extracellular space in microvesicular exosomes. J. Cell. Biochem. 105 (5), 1211–1218. https://doi.org/10.1002/jcb.21923.
Jiang, J., Nilsson-Ehle, P., Xu, N., 2006. Influence of liver cancer on lipid and lipoprotein metabolism. Lipids Health Dis. 5, 4. https://doi.org/10.1186/1476-511X-5-4.
Kalluri, R., LeBleu, V.S., 2020. The biology, function, and biomedical applications of exosomes. Science 367 (6478). https://doi.org/10.1126/science.aau6977.
Keller, M.D., Ching, K.L., Liang, F.X., Dhabaria, A., Tam, K., Ueberheide, B.M., Unutmaz, D., Torres, V.J., Cadwell, K., 2020. Decoy exosomes provide protection against bacterial toxins. Nature 579 (7798), 260–264. https://doi.org/10.1038/s41586-020-2066-6.
Khezri, M.R., Mohebalizadeh, M., Ghasemnejad-Berenji, M., 2023. Therapeutic potential of ADAM10 modulation in Alzheimer's disease: a review of the current evidence. Cell Commun. Signal. 21 (1), 60. https://doi.org/10.1186/s12964-023-01072-w.
Kokoglu, E., Karaarslan, I., Karaarslan, H.M., Baloglu, H., 1994. Alterations of serum lipids and lipoproteins in breast cancer. Cancer Lett. 82 (2), 175–178. https://doi.org/10.1016/0304-3835(94)90008-6.
Kottorou, A., Dimitrakopoulos, F.I., Diamantopoulou, G., Kalofonou, F., Stavropoulos, M., Thomopoulos, K., Makatsoris, T., Koutras, A., Kalofonos, H., 2023. Small extracellular vesicles (sEVs) biogenesis molecular players are associated with clinical outcome of colorectal cancer patients. Cancers (Basel) 15 (6). https://doi.org/10.3390/cancers15061685.
Kowal, J., Arras, G., Colombo, M., Jouve, M., Morath, J.P., Primdal-Bengtson, B., Dingli, F., Loew, D., Tkach, M., Thery, C., 2016. Proteomic comparison defines novel markers to characterize heterogeneous populations of extracellular vesicle subtypes. Proc. Natl. Acad. Sci. U. S. A. 113 (8), E968–E977. https://doi.org/10.1073/pnas.1521230113.
Kritchevsky, S.B., Wilcosky, T.C., Morris, D.L., Truong, K.N., Tyroler, H.A., 1991. Changes in plasma lipid and lipoprotein cholesterol and weight prior to the diagnosis of cancer. Cancer Res. 51 (12), 3198–3203. https://www.ncbi.nlm.nih.gov/pubmed/2039996.
Kumar, S., Senapati, S., Chang, H.C., 2024. Extracellular vesicle and lipoprotein diagnostics (ExoLP-Dx) with membrane sensor: a robust microfluidic platform to overcome heterogeneity. Biomicrofluidics 18 (4), 041301. https://doi.org/10.1063/5.0218986.
Kumar, S., Sinclair, J.A., Shi, T., Chuang, H.S., Senapati, S., Chang, H.C., 2025. Immunojanus Particles for low-volume and isolation-free unlabeled characterization of small Extracellular Vesicle in biofluids: characterization of disease type by surface marker profiling. bioRxiv Nat. Biomed. Eng. https://doi.org/10.1101/2024.08.17.607528 (in press).
Li, J., Zhang, Y., Dong, P.Y., Yang, G.M., Gurunathan, S., 2023. A comprehensive review on the composition, biogenesis, purification, and multifunctional role of exosome as delivery vehicles for cancer therapy. Biomed. Pharmacother. 165, 115087. https://doi.org/10.1016/j.biopha.2023.115087.
Maniya, N.H., Kumar, S., Franklin, J.L., Higginbotham, J.N., Scott, A.M., Gan, H.K., Coffey, R.J., Senapati, S., Chang, H.C., 2024. An anion exchange membrane sensor detects EGFR and its activity state in plasma CD63 extracellular vesicles from patients with glioblastoma. Commun. Biol. 7 (1), 677. https://doi.org/10.1038/s42003-024-06385-1.
Maretzky, T., Scholz, F., Koten, B., Proksch, E., Saftig, P., Reiss, K., 2008. ADAM10-mediated E-cadherin release is regulated by proinflammatory cytokines and modulates keratinocyte cohesion in eczematous dermatitis. J. Invest. Dermatol. 128 (7), 1737–1746. https://doi.org/10.1038/sj.jid.5701242.
Moshrefiravasjani, R., Kamrani, A., Nazari, N., Jafari, F., Nasiri, H., Jahanban-Esfahlan, R., Akbari, M., 2024. Exosome-mediated tumor metastasis: biology, molecular targets and immuno-therapeutic options. Pathol. Res. Pract. 254, 155083. https://doi.org/10.1016/j.prp.2023.155083.
Moss, M.L., Bomar, M., Liu, Q., Sage, H., Dempsey, P., Lenhart, P.M., Gillispie, P.A., Stoeck, A., Wildeboer, D., Bartsch, J.W., Palmisano, R., Zhou, P., 2007. The ADAM10 prodomain is a specific inhibitor of ADAM10 proteolytic activity and inhibits cellular shedding events. J. Biol. Chem. 282 (49), 35712–35721. https://doi.org/10.1074/jbc.M703231200.
Orme, J.J., Jazieh, K.A., Xie, T., Harrington, S., Liu, X., Ball, M., Madden, B., Charlesworth, M.C., Azam, T.U., Lucien, F., Wootla, B., Li, Y., Villasboas, J.C., Mansfield, A.S., Dronca, R.S., Dong, H., 2020. ADAM10 and ADAM17 cleave PD-L1 to mediate PD-(L)1 inhibitor resistance. OncoImmunology 9 (1), 1744980. https://doi.org/10.1080/2162402X.2020.1744980.
Pelegrini, L.N.C., Manzine, P.R., Popolin, C.P., Dorta, S., Grigoli, M.M., Alexandre-Silva, V., Pedroso, R., Ramos, A.A., Pott, H., Cominetti, M.R., 2025. Higher soluble ADAM10 plasma levels are associated with decreased cognitive performance in older adults carrying APOEepsilon4. Neurobiol. Aging 151, 70–75. https://doi.org/10.1016/j.neurobiolaging.2025.04.003.
Rosenbaum, D., Saftig, P., 2024. New insights into the function and pathophysiology of the ectodomain sheddase A Disintegrin and Metalloproteinase 10 (ADAM10). FEBS J. 291 (13), 2733–2766. https://doi.org/10.1111/febs.16870.
Sabatke, B., Rossi, I.V., Sana, A., Bonato, L.B., Ramirez, M.I., 2023. Extracellular vesicles biogenesis and uptake concepts: a comprehensive guide to studying host-pathogen communication. Mol. Microbiol. https://doi.org/10.1111/mmi.15168.
Safavi-Sohi, R., Johnson, J., Liu, Y., Yang, J., Hilliard, T.S., Wang, Z., Barile, C., Mijares, J., Wang, C., Chang, H.C., Whelan, R.J., Stack, M.S., 2025. Peritoneal cavity-derived small extracellular vesicles from aged tumor-naive hosts promote ovarian cancer adhesion and invasion. Cell Commun. Signal. 23 (1), 308. https://doi.org/10.1186/s12964-025-02273-1.
Saha, N., Baek, D.S., Mendoza, R.P., Robev, D., Xu, Y., Goldgur, Y., De La Cruz, M.J., de Stanchina, E., Janes, P.W., Xu, K., Dimitrov, D.S., Nikolov, D.B., 2023. Fully human monoclonal antibody targeting activated ADAM10 on colorectal cancer cells. Biomed. Pharmacother. 161, 114494. https://doi.org/10.1016/j.biopha.2023.114494.
Sakamoto, K., Jin, S.P., Goel, S., Jo, J.H., Voisin, B., Kim, D., Nadella, V., Liang, H., Kobayashi, T., Huang, X., Deming, C., Horiuchi, K., Segre, J.A., Kong, H.H., Nagao, K., 2021. Disruption of the endopeptidase ADAM10-Notch signaling axis leads to skin dysbiosis and innate lymphoid cell-mediated hair follicle destruction. Immunity 54 (10), 2321–2337 e2310. https://doi.org/10.1016/j.immuni.2021.09.001.
Seifert, A., Dusterhoft, S., Wozniak, J., Koo, C.Z., Tomlinson, M.G., Nuti, E., Rossello, A., Cuffaro, D., Yildiz, D., Ludwig, A., 2021. The metalloproteinase ADAM10 requires its activity to sustain surface expression. Cell. Mol. Life Sci. 78 (2), 715–732. https://doi.org/10.1007/s00018-020-03507-w.
Shao, Y., Chen, T., Zheng, X., Yang, S., Xu, K., Chen, X., Xu, F., Wang, L., Shen, Y., Wang, T., Zhang, M., Hu, W., Ye, C., Yu, X., Shao, J., Zheng, S., 2018. Colorectal cancer-derived small extracellular vesicles establish an inflammatory premetastatic niche in liver metastasis. Carcinogenesis 39 (11), 1368–1379. https://doi.org/10.1093/carcin/bgy115.
Sharma, H., Yadav, V., Burchett, A., Shi, T., Senapati, S., Datta, M., Chang, H.C., 2025. A Mem-dELISA platform for dual color and ultrasensitive digital detection of colocalized proteins on extracellular vesicles. Biosens. Bioelectron. 267, 116848. https://doi.org/10.1016/j.bios.2024.116848.
Sharma, H., Yadav, V., D'Souza-Schorey, C., Go, D.B., Senapati, S., Chang, H.C., 2023. A scalable high-throughput isoelectric fractionation platform for extracellular nanocarriers: comprehensive and bias-free isolation of ribonucleoproteins from Plasma, urine, and saliva. ACS Nano 17 (10), 9388–9404. https://doi.org/10.1021/acsnano.3c01340.
Sowemimo-Coker, S.O., 2002. Red blood cell hemolysis during processing. Transfus. Med. Rev. 16 (1), 46–60. https://doi.org/10.1053/tmrv.2002.29404.
Spugnini, E.P., Logozzi, M., Di Raimo, R., Mizzoni, D., Fais, S., 2018. A role of tumor-released exosomes in paracrine dissemination and metastasis. Int. J. Mol. Sci. 19 (12). https://doi.org/10.3390/ijms19123968.
Surman, M., Stepien, E., Hoja-Lukowicz, D., Przybylo, M., 2017. Deciphering the role of ectosomes in cancer development and progression: focus on the proteome. Clin. Exp. Metastasis 34 (3-4), 273–289. https://doi.org/10.1007/s10585-017-9844-z.
[webpage]. Survival Rates for Colorectal Cancer, 2025. American Cancer Society. https://www.cancer.org/cancer/types/colon-rectal-cancer/detection-diagnosis-staging/survival-rates.html.
Tellier, E., Canault, M., Rebsomen, L., Bonardo, B., Juhan-Vague, I., Nalbone, G., Peiretti, F., 2006. The shedding activity of ADAM17 is sequestered in lipid rafts. Exp. Cell Res. 312 (20), 3969–3980. https://doi.org/10.1016/j.yexcr.2006.08.027.
Tugutova, E.A., Tamkovich, S.N., Patysheva, M.R., Afanas'ev, S.G., Tsydenova, A.A., Grigor'eva, A.E., Kolegova, E.S., Kondakova, I.V., Yunusova, N.V., 2019. Relation between Tetraspanin- associated and Tetraspanin- Non- associated exosomal proteases and metabolic syndrome in colorectal cancer patients. Asian Pac. J. Cancer Prev. APJCP 20 (3), 809–815. https://doi.org/10.31557/APJCP.2019.20.3.809.
[webpage]. U.S. Cancer Statistics Colorectal Cancer Stat Bite, 2025. U.S. Department of Health and Human Services. Centers for Disease Control and Prevention. https://www.cdc.gov/united-states-cancer-statistics/publications/colorectal-cancer-stat-bite.html.
Van Daela, T.H.S.V., Nopens, I., 2015. pyIDEAS: an open source python package for model analysis. Comput. Aided Chem. Eng. 37, 569–574. https://doi.org/10.1016/B978-0-444-63578-5.50090-6.

van Duijnhoven, F.J.B., Bueno-De-Mesquita, H.B., Calligaro, M., Jenab, M., Pischon, T., Jansen, E.H.J.M., Frohlich, J., Ayyobi, A., Overvad, K., Toft-Petersen, A.P., Tjønneland, A., Hansen, L., Boutron-Ruault, M.-C., Clavel-Chapelon, F., Cottet, V., Palli, D., Tagliabue, G., Panico, S., Tumino, R., Vineis, P., Kaaks, R., Teucher, B., Boeing, H., Drogan, D., Trichopoulou, A., Lagiou, P., Dilis, V., Peeters, P.H.M., Siersema, P.D., Rodríguez, L., González, C.A., Molina-Montes, E., Dorronsoro, M., Tormo, M.-J., Barricarte, A., Palmqvist, R., Hallmans, G., Khaw, K.-T., Tsilidis, K.K., Crowe, F.L., Chajes, V., Fedirko, V., Rinaldi, S., Norat, T., Riboli, E., 2011. Blood lipid and lipoprotein concentrations and colorectal cancer risk in the European Prospective Investigation into Cancer and Nutrition. Gut 60 (8), 1094–1102. https://doi.org/10.1136/gut.2010.225011.

Wetzel, S., Seipold, L., Saftig, P., 2017. The metalloproteinase ADAM10: a useful therapeutic target? Biochim. Biophys. Acta Mol. Cell Res. 1864 (11 Pt B), 2071–2081. https://doi.org/10.1016/j.bbamcr.2017.06.005.

Wu, L., Zhang, X., Zhang, B., Shi, H., Yuan, X., Sun, Y., Pan, Z., Qian, H., Xu, W., 2016. Exosomes derived from gastric cancer cells activate NF-kappaB pathway in macrophages to promote cancer progression. Tumour Biol. 37 (9), 12169–12180. https://doi.org/10.1007/s13277-016-5071-5.

Xiang, Z., Wang, Y., Ma, X., Song, S., He, Y., Zhou, J., Feng, L., Yang, S., Wu, Y., Yu, B., Xia, G., Xu, W., Zhao, Y., Wang, L., 2025. Targeting the NOTCH2/ADAM10/TCF7L2 axis-mediated transcriptional regulation of Wnt Pathway suppresses tumor growth and enhances chemosensitivity in colorectal cancer. Adv. Sci. (Weinh.) 12 (3), e2405758. https://doi.org/10.1002/advs.202405758.

Xiong, M., Zhang, Q., Hu, W., Zhao, C., Lv, W., Yi, Y., Wu, Y., Wu, M., 2020. Exosomes from adipose-derived stem cells: the emerging roles and applications in tissue regeneration of plastic and cosmetic surgery. Front. Cell Dev. Biol. 8, 574223. https://doi.org/10.3389/fcell.2020.574223.

Xu, R., Rai, A., Chen, M., Suwakulsiri, W., Greening, D.W., Simpson, R.J., 2018. Extracellular vesicles in cancer - implications for future improvements in cancer care. Nat. Rev. Clin. Oncol. 15 (10), 617–638. https://doi.org/10.1038/s41571-018-0036-9.

Yuan, X.Z., Sun, S., Tan, C.C., Yu, J.T., Tan, L., 2017. The role of ADAM10 in Alzheimer's Disease. J. Alzheimers Dis. 58 (2), 303–322. https://doi.org/10.3233/JAD-170061.

Zhang, P., Wu, X., Gardashova, G., Yang, Y., Zhang, Y., Xu, L., Zeng, Y., 2020. Molecular and functional extracellular vesicle analysis using nanopatterned microchips monitors tumor progression and metastasis. Sci. Transl. Med. 12 (547). https://doi.org/10.1126/scitranslmed.aaz2878.

Zhao, H., Yang, L., Baddour, J., Achreja, A., Bernard, V., Moss, T., Marini, J.C., Tudawe, T., Seviour, E.G., San Lucas, F.A., Alvarez, H., Gupta, S., Maiti, S.N., Cooper, L., Peehl, D., Ram, P.T., Maitra, A., Nagrath, D., 2016. Tumor microenvironment derived exosomes pleiotropically modulate cancer cell metabolism. eLife 5, e10250. https://doi.org/10.7554/eLife.10250.

Zheng, X., Bahr, M., Doeppner, T.R., 2019. From Tumor metastasis towards cerebral ischemia-extracellular vesicles as a general concept of intercellular communication processes. Int. J. Mol. Sci. 20 (23). https://doi.org/10.3390/ijms20235995.